HIGH-RESOLUTION LAND/ICE IMAGING USING SEASAT SCATTEROMETER MEASUREMENTS

D. G. Long[1], P. T. Whiting[1], P. J. Hardin[2]

[1]Electrical and Computer Engineering Department, [2]Geography Department
Brigham Young University, Provo, UT 84602

ABSTRACT

In this paper we introduce a new method for obtaining high resolution images (to 4 km) of the land backscatter from low-resolution Seasat-A scatterometer (SASS) measurements. The method utilizes the measurement cell overlap in multiple spacecraft passes over the region of interest and signal processing techniques to generate high resolution images of the radar backscatter. The overlap in the σ^o resolution cells is exploited to estimate the underlying high resolution surface radar backscatter characteristics using a robust new multivariate image reconstruction algorithm. The new algorithm has been designed to operate in the high noise environment typical of scatterometer measurements. The ultimate resolution obtainable is a function of the number of measurements and the measurement overlap. We describe the method and provide sample results based on SASS data. We describe modifications to future scatterometers which would permit the method to produce 1-2 km resolution over land and ice. The high-resolution scatterometer imaging technique, coupled with the frequent, multiple-incidence angle coverage afforded by the scatterometer, is expected to significantly enhance the utility of scatterometer data in various land, ice, and vegetation studies.

INTRODUCTION

Spaceborne wind scatterometers are an important element in future remote sensing systems because of their proven ability to make all-weather measurements of vector winds over the ocean. Current and planned scatterometer designs have resolutions in the 25-50 km range which is sufficient for the study of oceanic winds. While scatterometers make measurements of the normalized radar backscatter coefficient (σ^o) over land, these measurements have been used primarily for calibration of the instrument [1].

Spaceborne wind scatterometers observe σ^o over a wide range of incidence angles. Over an incidence angle (θ) range of $[20°, 57°]$, the dependence of σ^o on the incidence angle is linear, i.e., [1]

$$10\log_{10}\sigma^o(\theta) = \mathcal{A} - \mathcal{B}(\theta - 40°) \tag{1}$$

where $\mathcal{A}$ and $\mathcal{B}$ are constants independent of θ. $\mathcal{A}$ is the value of σ^o at an incidence angle of 40°. $\mathcal{A}$ can thus be considered to be the "incidence angle-normalized" σ^o. Because of the wide range of measurement incidence angles used by wind scatterometers, the $\mathcal{A}$ and $\mathcal{B}$ coefficients of this model are used in lieu of σ^o.

The coarse resolution (nominally 50 km) of the SASS measurements is a significant limitation to the application of the SASS data in land and ice studies. To ameliorate this difficulty we have developed a new method for obtaining high-resolution estimates of $\mathcal{A}$ and $\mathcal{B}$ from SASS-class scatterometer measurements. The technique can achieve even higher resolution for future scatterometers such as the NASA Scatterometer (NSCAT). This paper describes our approach and results.

HIGH-RESOLUTION IMAGING METHOD

SASS obtained two measurements of σ^o at different azimuth angles using multiple antennas. The σ^o measurement resolution "cells" were (approximately) six-sided polygons with variable size on an irregular grid. The σ^o measurements were noisywith a normalized standard deviation (K_p) of 4% to 50%+ over land.

Our method for generating high-resolution images of $\mathcal{A}$ and $\mathcal{B}$ from low resolution scatterometer measurements is based on the measurement overlap from multiple SASS passes. The method is described in detail in [3]. A summary is provided below.

The method produces estimates of $\mathcal{A}$ and $\mathcal{B}$ on a rectilinear grid. Figure 1 illustrates a six-sided σ^o cell imposed on this small-scale grid of high-resolution elements. Assuming a noise-free measurement, the value of σ^o observed by the scatterometer (denoted by ϱ_k where k is the measurement number) is a weighted average of the σ^o's of the individual high-resolution elements covered by the measurement, i.e.,

$$\varrho_k = \sum_{c=L_k}^{R_k}\sum_{a=B_k}^{T_k} h(c,a;k)\sigma^o(c,a;k) \tag{2}$$

where L_k, R_k, T_k, and B_k define a bounding rectangle for the k^{th} hexagonal σ^o measurement cell, $h(c,a;k)$ is the weighting function for the $(c,a)^{th}$ high-resolution element, and $\sigma^o(c,a;k)$ is the σ^o value for the $(c,a)^{th}$ high-resolution element. The incidence angle dependence of σ^o and h is subsumed in the k index. [In Eq. (2) c denotes the cross-track dimension while a denotes the along-track dimension.] Over a given scatterometer measurement cell the incidence angle θ can be assumed to be approximately constant. The actual scatterometer measurements, z_k, are noisy, i.e.,

$$z_k = \varrho_k(1 + \nu_k) \tag{3}$$

where ν_k is a zero-mean Gaussian noise with variance K_{Pk}^2.

The high-resolution reconstruction problem can then be posed as: Given noisy measurements z_k of ϱ_k for $k \in [1, N]$, determine $\mathcal{A}(c,a)$ and $\mathcal{B}(c,a)$ for each element of the high-resolution grid.

To solve this problem consider an $N_c \times N_a$ element region of the resolution grid. Collecting all the measurements whose bounding rectangles are completely contained within the region of interest, we obtain a matrix equation relating the measurements z_k (in Z) to $\sigma^o(c,a)$ (in S)

$$Z = HS + \mathcal{V} \tag{4}$$

where Z is an N-dimensional vector, H is an $N \times M$ ($M = N_cN_a$) matrix containing the $h(c,a;k)$, S is an M-dimensional vector of $\sigma^o(c,a)$ in lexicographic order (i.e., $s_n = \sigma^o(c,a)$ where $n = c + aN_c$) and $\mathcal{V}$ contains the noise terms ν_k. Depending on the resolution element size and the number of measurements z_k, H can be either over- or under-determined. The elements of the matrix H are computed by determining the intersection of the six-sided integrated σ^o measurements and the high-resolution elements (see Fig. 1). For appropriately sized high-resolution elements, we can assume that the entries of H are either 1 or 0.

We note that if the high-resolution element size is very small or the overlap in the measurements is insufficient, H will be underdetermined. While our approach results in a unique solution for S, the resulting estimate may be *smoothed* so that the *effective* resolution (defined as the minimum resolvable feature size) may actually be larger than the desired pixel size. Thus, the ultimate resolution achievable in the reconstruction is limited by the rank of H and therefore by the measurement cell overlap and the number of measurements. Reducing the size of the high-resolution elements arbitrarily will not increase the effective resolution of the resulting estimate but it may increase the estimate noise.

Increasing the number of measurements, which also increases the measurement overlap, will improve the ultimate resolution. However, for SASS this implies that more orbits must be used to generate the image for which we must assume that the target characteristics remain fixed. We must also assume that σ^o is not a function of azimuth angle and is not affected by topography. These assumptions are explored in greater detail in [4,5]. In this paper we have used the entire three-month SASS data set to generate images of $\mathcal{A}$ and $\mathcal{B}$ over a test region in the Amazon basin at a resolution of $1/26° \times 1/26°$. For many areas of the extended Amazon basin, satisfactory images can be produced with better resolution and/or shorter time scales.

Our multivariate iterative approach to solving Eq. (4) is based on algebraic reconstruction techniques (ART). An initial $\mathcal{B}$ estimate image, B^0, is made by setting $b_i^0 = -0.13$ (the global average of $\mathcal{B}$).

91-72810/92$03.00 © IEEE 1992

The initial $\mathcal{A}$ image is set to zero, i.e., $s_i^0 = 0$. In the k^{th} iteration, the previous $\mathcal{B}$ estimate image is used to generate an estimate of $\mathcal{A}$. Linear regression of the $\mathcal{A}$ update terms (expressed at the original measurement incidence angle) is then used to update the previous estimate of $\mathcal{B}$. To improve noise tolerance, both the new $\mathcal{A}$ and $\mathcal{B}$ estimates are determined as a non-linearly weighted average of the previous estimates and the estimate update.

With the measurements, z_j, expressed in dB the scatterometer image reconstruction (SIR) algorithm follows. Let

$$f_j^k = 10\log_{10}\left[\frac{1}{p_i}\sum_{n=1}^{N} h_{jn}10^{s_n^k/10}\right], \quad p_i = \sum_{m=1}^{N} h_{mi}, \quad \text{and} \tag{5}$$

$$d_{ij}^k = \left(\frac{z_j - b_i^k(\theta_j - 40°)}{f_j^k}\right)^w. \tag{6}$$

The $\mathcal{A}$ estimate update term, u_{ij}^k, is then computed as

$$u_{ij}^k = \begin{cases} \left[\frac{1}{2}\frac{1}{f_j^k}\left(1 - \frac{1}{d_{ij}^k}\right) + \frac{1}{s_i^k d_{ij}^k}\right]^{-1} & d_{ij}^k \geq 1 \\ \left[\frac{1}{2}f_j^k\left(1 - d_{ij}^k\right) + s_i^k d_{ij}^k\right] & d_{ij}^k < 1 \end{cases} \tag{7}$$

with the $\mathcal{A}$ estimate, s_i^k, updated according to

$$s_i^{k+1} = \frac{1}{p_i}\sum_{j=1}^{N} h_{ji}u_{ij}^k. \tag{8}$$

To compute the $\mathcal{B}$ estimate, let $\zeta_{ij}^k = u_{ij}^k + b_i^k(\theta_j - 40°)$ and

$$r_i = \sum_{j=1}^{N} h_{ji}\theta_j^2 \quad t_i = \sum_{j=1}^{N} h_{ji}\theta_j. \tag{9}$$

Linear regression of the $\mathcal{A}$ updates, u_{ij}^k, provides an update for $\mathcal{B}$,

$$c_i^k = \frac{1}{p_i r_i - t_i^2}\left(p_i\sum_{j=1}^{N} h_{ji}\theta_j\zeta_{ij}^k - t_i\sum_{j=1}^{N} h_{ji}\zeta_{ij}^k\right). \tag{10}$$

However, this update is only usable if the range of incidence angles (θ_j) is sufficiently wide. Since a wider incidence angle range implies greater confidence in the $\mathcal{B}$ estimate update, the $\mathcal{B}$ estimate is updated using a weighted average of c_i^k and the previous $\mathcal{B}$ estimate. The weighting factor is a simple function of the variance of θ. To compute it let

$$r = \frac{p_i}{t_i^2}\sum_{j=1}^{N} h_{ji}\theta_j^2 - 1 \tag{11}$$

then the $\mathcal{B}$ estimate image is updated according to

$$b_i^{k+1} = \frac{1}{r+1}\left(rc_i^k + b_i^k\right). \tag{12}$$

This system of equations is iterated over k until convergence. Unlike conventional ART algorithms which are sensitive to noise and diverge if iterated too many times, the SIR algorithm is relatively noise-tolerant and does not diverge after continued iteration. Instead, as the algorithm converges the update terms continue to grow smaller until there is no change between iterations. The algorithm has been tested extensively using simulated and actual SASS measurements and typically converges within 30-40 iterations.

We observed that the subjective quality of the final images may be improved by applying an edge-preserving 3×3 median filter. It was further observed that the image noise can be significantly reduced, with only a small reduction in the image resolution, by application of a hybrid median-linear filter to the image estimates at each stage of the iteration [3]. The SIR algorithm with the added filtering is termed SIRF.

SASS EXAMPLE

The SIRF algorithm was used with actual SASS σ^o measurements to generate high-resolution maps of $\mathcal{A}$ and $\mathcal{B}$ over a test region over the Guiana Highlands in South America. A wider view of the whole Amazon basin is given in [5]. σ^o measurements with excessive K_p ($K_p > 15\%$) were excluded. Only σ^o measurements with incidence angles in the range 23° to 57° were used. The resulting $\mathcal{A}$ image is shown in Fig. 2. The high-resolution elements are $1/26° \times 1/26°$. A $0.5° \times 0.5°$ ($\sim$ 50 km—the intrinsic resolution of SASS) $\mathcal{A}$ image generated using the "binning" method of [2] is shown in Fig. 3. The resolution enhancement of the SIRF algorithm relative to the "binning" approach is clearly evident. In constrast to the $\mathcal{A}$ images, the $\mathcal{B}$ images (not shown) show only limited spatial detail (see [4]).

The low $\mathcal{A}$ (black and dark grey) area in Fig. 2 corresponds to tall grassland (black) with broadleafed evergreen trees and shrubs (dark grey). An area of tropical forest immediately north of the dark region appears as shades of light gray on the image. Smaller areas of lowland forest also appear as dark areas along the north central portions of the image. The light areas correspond to very moist multi-canopied tropical forest. Based on [4], the $\mathcal{A}$ value appears to be most closely related to vegetation canopy density.

APPLICATIONS TO FUTURE SCATTEROMETERS

While the best obtainable resolution with this method using SASS data can be considered only "high-resolution" when compared to the intrinsic 50 km resolution of the scatterometer, much higher resolution is possible by modifying future scatterometers. As presented here, high-resolution scatterometry is based on measurement cell overlap. For SASS, overlap was obtained by combining multiple orbits over an extended period of time. Increasing the number of orbits combined results in improved resolution and reduced estimate noise. However, the target's radar characteristics must remain constant over the data acquisition interval. This represents a serious limitation for rapidly changing regions such as polar ice.

For future Doppler scatterometers such as NSCAT and the NSCAT-class scatterometer planned for the EoS-era, significant resolution enhancement resulting from measurement overlap can be obtained by modifying the measurement sequence. This permits high-resolution imaging with only a single spacecraft pass, relaxing the target constancy requirement. Over land and ice the ultimate resolution attainable is 1-2 km. The required instrument modifications, described in detail in [3], are relatively minor. They consist of modifying the beam sequence timing and downlinking the periodogram data. This increases the data rate from 3.1 kbps to 750 kbps but does not affect the wind measurement capability. The higher-rate data need only be collected over land and ice.

CONCLUSION

Traditionally, spaceborne scatterometers have been low-resolution radar instruments designed to measure winds over the ocean. Because of their low resolution, the scatterometer measurements made over land have been used primarily to calibrate the instrument. However, improved resolution would enhance the scientific utility of the scatterometer data for land and ice studies. Over ice, the frequent, multi-incidence angle, high-resolution scatterometer measurements may permit determination of ice-age and snow cover. Coupled with radiometer measurements this may result in significant improvements in the understanding of the polar heat flux.

In this paper we have described a method for obtaining high-resolution radar images from scatterometer measurements. The technique is based on spatial measurement overlap and a new image reconstruction algorithm. Resolution enhancement of 8-10 times was achieved using actual SASS data. The resulting medium-scale is useful in a variety of other geophysical studies, e.g., vegetation classification [4,5] and ice studies [6].

The limitations of our technique when applied to SASS data may be ameliorated for future Doppler scatterometers such as NSCAT and the NSCAT-class EoS-era scatterometer. With relatively inexpensive modifications, future NSCAT-class scatterometers can achieve effective resolutions as low as 1-2 km. Thus, the modified scatterometer can provide significant additional science return with only a limited budgetary impact. This relatively inexpensive enhancement of planned missions may yield significant contributions to future studies of global change.

While our technique was developed expressly for spaceborne scatterometer measurements, it can be applied to other sensors such as radiometers.

ACKNOWLEDGEMENTS

We wish to acknowledge the support of the NASA Headquarters programs in Physical Oceanography (Gary Lagerloef and David Adamec) and Polar Sciences (Robert Thomas). The SASS GDR data was obtained from the NASA Ocean Data System at the Jet Propul-

sion Laboratory/California Institute of Technology. We acknowlege the aid of Gary Skouson in preparing the SASS data.

REFERENCES

[1] J. W. Johnson, L. A. Williams, Jr., E. M. Bracalente, F. B. Beck, and W. L. Grantham, "Seasat-A Satellite Scatterometer Instrument Evaluation," *IEEE J. Oceanic Eng.*, Vol. OE-5, No. 2, pp. 138-144, April 1980.

[2] R. G. Kennett and F. K. Li, "Seasat Over-Land Scatterometer Data, Part II: Selection of Extended Area Land-Target Sites for the Calibration of Spaceborne Scatterometers," *IEEE Trans. Geosci. Remote Sensing*, Vol. GE-27, No. 6, pp. 779-788, Nov. 1989.

[3] D. G. Long, P. J. Hardin, and P. T. Whiting, "High-Resolution Imaging of Land/Ice Using Spaceborne Scatterometry Part I: The Imaging Technique," submitted to *IEEE Trans. Geosci. Remote Sensing*, 1992.

[4] D. G. Long and P. J. Hardin, "High-Resolution Imaging of Land/Ice Using Spaceborne Scatterometry Part II: Vegetation Studies of the Amazon Basin and Other Applications," submitted to *IEEE Trans. Geosci. Remote Sensing*, 1992.

[5] P. J. Hardin and D. G. Long, "Land Imaging with Reconstructed High-Resolution Seasat-A Scatterometer Data: An Amazon Experiment," *IGARSS'92*, 1992.

[6] D. G. Long, P. J. Hardin, and R. A. Shaw, "Greenland Observed at High Resolution by the Seasat Scatterometer," *IGARSS '92*, 1992.

Figure 1. Illustration showing an integrated SASS σ^o cell overlaying the high resolution grid. Only the shaded square grid elements will have non-zero $h(c,a;k)$. The bounding rectangle is also indicated.

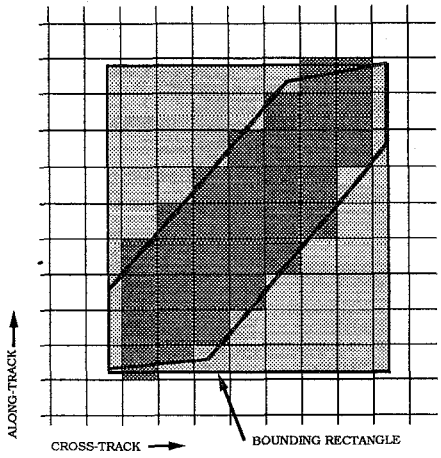

Figure 2. a) $\mathcal{A}$ image of the Amazon test region from actual vertically-polarized SASS data using the SIRF algorithm.

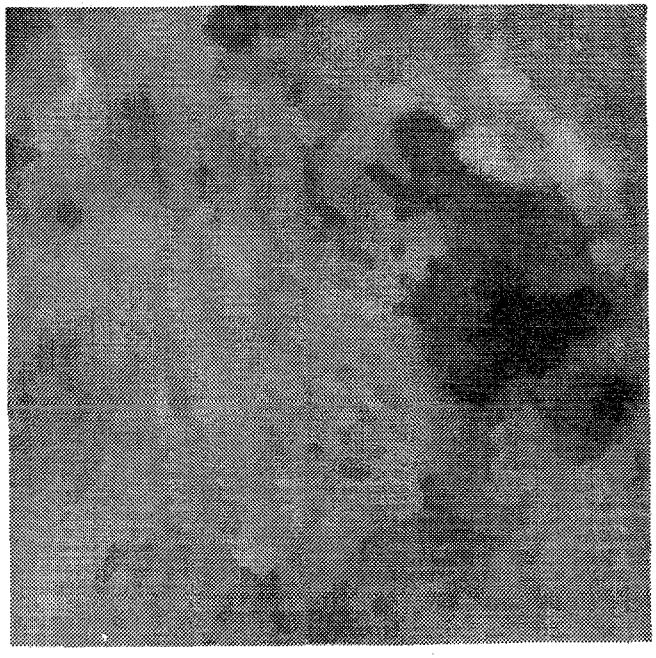

Figure 3. $\mathcal{A}$ image generated from the same SASS measurements as Fig.2 but using the "binning" approach. Resolution is $0.5° \times 0.5°$.